Uptake and retention of molybdenum in cementitious systems

Steve Lange[1]*, Martina Klinkenberg[1], Juri Barthel[2], Dirk Bosbach[1], Guido Deissmann[1]

[1]Institute of Energy and Climate Research (IEK-6): Nuclear Waste Management and Reactor Safety, Forschungszentrum Jülich GmbH, Jülich, Germany

[2]Ernst Ruska-Centre for Microscopy and Spectroscopy with Electrons (ER-C 2), Forschungszentrum Jülich GmbH, Jülich, Germany

*Corresponding author.

E-mail address: steve_lange@gmx.de (Steve Lange).

Abstract

The uptake of molybdenum, present in aqueous cementitious environments in the form of the molybdate ion (MoO_4^{2-}), by various cement hydration phases such as calcium-silicate-hydrates (C-S-H), monosulfate (AFm), ettringite (AFt), as well as hardened cement paste made from Ordinary Portland cement (OPC), was studied in batch-type sorption experiments under anoxic conditions. Uptake kinetics were generally fast, leading to sorption equilibrium in less than 30 days. In particular, a strong uptake of molybdate by AFm phases was observed as well as a distinct contribution of C-S-H phases to the molybdate retention in cementitious systems, the latter depending on the Ca/Si-ratio of the C-S-H and the alkali content in solution. In systems containing hydrogarnet, the neo-formation of a molybdate-bearing AFm phase was identified as an additional process contributing to molybdate retention. The findings have implications for selecting grouts for the immobilisation of radioactive waste streams containing Mo-93 and also enhance the data available on molybdate sorption and retention in cementitious systems.

Key words: cementitious materials, molybdate retention, sorption, uptake mechanisms

1. Introduction

Cement-based materials have a wide range of uses in nuclear waste management, for example, as construction and backfill materials in near-surface repositories and geological disposal facilities, as an immobilisation matrix for low- and intermediate-level wastes, and in specific waste containers (*e.g.*, Atkins and Glasser, 1992; Bel et al., 2006; Drace and Ojovan, 2013, Glasser, 1997, 2001, 2011; Jantzen et al., 2010). This is in particular due to the general

radionuclide fixation and immobilisation properties of cementitious materials (including the low solubility of many metals at high pH) and their low permeability and diffusivity, as well as their versatility and maturity in application. After hydration and curing, cementitious materials represent heterogeneous mixtures of various hydration phases, comprising mainly nanocrystalline calcium-silicate-hydrates (C-S-H), in addition to calcium aluminate/ferrate compounds (AFm/AFt), portlandite ($Ca(OH)_2$) and other minor phases such as hydrotalcite (*cf.* Glasser, 2001; Taylor, 1997). The amount and composition of the hydration phases (*e.g.*, Ca/Si ratio or Al content in C-S-H) in a given cementitious material and its transport properties (*e.g.* porosity, diffusivity) depend strongly on the cement formulation and the mixing and curing processes and conditions (Taylor, 1997). Moreover, phase assemblage, microstructure, and porewater composition of the cementitious materials employed in nuclear waste repositories will evolve over time, due to interaction with groundwaters. This leads to a decrease of porewater pH and alkalinity and changes in the hydration phases (*e.g.*, depletion of portlandite, decrease of Ca/Si-ratio in C-S-H phases) in several stages in the long term (*e.g.*, Beattie and Williams, 2012; Berner, 1992; Drace and Ojovan, 2013; Glasser, 2011; Hoch et al., 2012), with the pore water pH finally approaching the pH of the surrounding groundwater.

The retention of radionuclides in cement-based materials can be attributed to three principal mechanisms: surface sorption to hydration phases or aggregates, incorporation into existing or newly formed phases (by entrapment or formation of solid solutions), and precipitation of sparingly soluble pure phases (*cf.* Evans, 2008; Jantzen et al., 2010; Ochs, et al., 2016). Thus, the ability of a cementitious grout or backfill material to retain a specific radionuclide will vary, depending on the chemical speciation and valence state of the radionuclide and the type and degradation state of the cementitious material, the conditions in the pore water (*e.g.* with respect to pH and redox conditions, ionic strength and cation/anion concentrations), and the presence of additives such as superplasticisers (*e.g.*, Ochs et al., 2016). The retention of radionuclides in complex cementitious materials has been addressed in a large number of studies over the last decades (*e.g.*, see reviews by Evans, 2008; Gougar et al., 1996; Glasser, 1997, 2011; Jantzen et al., 2010), often on a mainly phenomenological basis, resulting in the compilation of various sorption coefficient databases (*e.g.*, Heath et al., 2000; Ochs et al., 2016; Wang et al., 2013; Wieland, 2014; Wieland and Van Loon, 2002). However, the mechanisms governing the immobilisation of

various safety-relevant radionuclides by cementitious materials on the molecular scale are still not completely understood.

Molybdenum-93 (Mo-93) has a half-life of 4,000 years (Brown et al., 2018) and decays by electron capture to stable Nb-93. It is generated in nuclear power plants by neutron activation of the stable molybdenum isotope Mo-92 present in particular in metallic reactor components such as stainless steels, and can thus occur in various nuclear waste streams. Molybdenum is a redox-sensitive element, whose aqueous speciation under neutral to highly alkaline conditions is dominated by the thermodynamically highly stable molybdate (MoO_4^{2-}) oxo-anion (*cf.* Fig. 1, left). Under cementitious conditions, powellite ($CaMoO_4$) is thought to be the solubility-limiting Mo phase, depending on redox potential and the dissolved Ca concentration. In the presence of portlandite (*i.e.* at pH ≥ 12.5) representative of degradation stages I and II of cementitious materials (*cf.* Drace and Ojovan, 2013; Glasser, 2011; Hoch et al., 2012; Ochs et al., 2016), the maximum dissolved Mo concentrations controlled by powellite are expected to be in the order of 10^{-6} to 10^{-4} mol kg^{-1} (*cf.* Fig. 1, right).

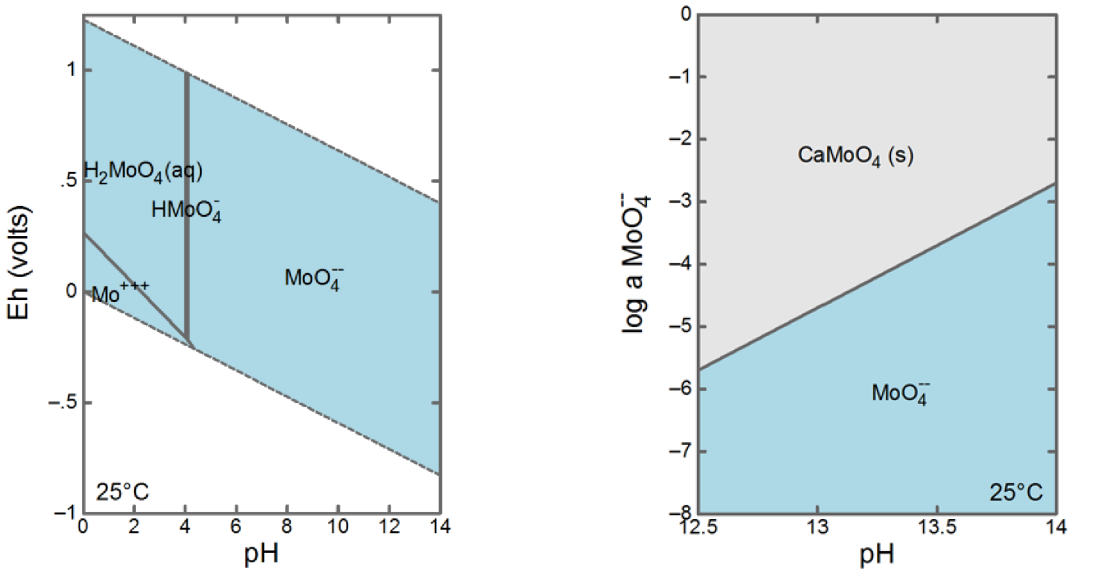

Fig. 1. (left) Eh-pH diagram for aqueous Mo species (a Mo = 10^{-9}, precipitation of solids suppressed in calculation); (right) solubility of powellite ($CaMoO_4$) in the presence of portlandite ($Ca(OH)_2$). Thermodynamic database: ThermoChimie Version 9b0 (Giffaut et al., 2014; Grivé et al., 2015).

The interaction of Mo with cementitious materials has received relatively little attention in the past. Due to the scarcity of molybdate sorption data on hardened cement paste (HCP),

Ochs et al. (2016) suggested the use of selenate (SeO_4^{2-}) as an analogue. The retention of molybdate in cementitious systems is assumed to be due to the substitution of sulphate in ettringite and AFm phases, besides precipitation of powellite at higher Mo concentrations (Evans, 2008; Glasser, 2002, Kindness et al., 1994; Ochs et al., 2002, 2016; Zhang, 2000, Zhang and Reardon, 2003). Recently, Ma et al. (2017) and Marty et al. (2018) explored in detail the mechanisms of molybdenum uptake by AFm phases, providing evidence for various sorption modes depending on the Mo concentration in solution and the competitive effect of OH^- ions on molybdate uptake. However, the potential role of other hydration phases such as C-S-H with respect to molybdate retention still remains open (Lidman et al., 2017). Thus, the retention of Mo in cementitious systems was one issue addressed within the framework of the European CEBAMA project (*cf*. Grambow et al., 2020). Within this context, the aim of the present work was to further the mechanistic understanding of the interaction of molybdate with cementitious materials. A bottom-up approach was adopted to explore the contribution of the various phases present in HCP to the retention of molybdate, studying both the interaction of Mo with synthesised single cement hydrations phases representative of those in hydrated cements, as well as with HCP itself. Besides sorption kinetics, the effects of solution chemistry were explored using different solution compositions reflecting the porewater in HCP at different stages of degradation.

2. Materials and methods

2.1 Synthesis of model hydration phases

The synthesised cement hydration phases comprised C-S-H with Ca/Si ratios of 0.9 and 1.4 (subsequently termed C-S-H0.9 and C-S-H1.4, respectively), AFm phases ($Ca_4Al_2(OH)_{12}(X^{2-})\cdot 6H_2O$) containing sulphate and carbonate as anions in the interlayer, respectively, ettringite (AFt, $Ca_6Al_2(SO_4)_3(OH)_{12}\cdot 26H_2O$), hydrogarnet ($C_3AH_6$, $Ca_3Al_2(OH)_{12}$), portlandite ($Ca(OH)_2$), and calcite ($CaCO_3$). The syntheses of these phases followed established procedures from the literature (*i.e.*, C-S-H: Atkins et al. 1992; AFm: Baur at al., 2004; Matschei et al., 2006; AFt: Atkins et al., 1991; Baur at al., 2004); the procedures are described in detail in Lange et al. (2018) and Lange (2019). To avoid carbonation of the phases, synthesis and also sample preparation and storage were performed in a glove box under argon atmosphere (< 10 ppm CO_2).

Molybdate-containing AFm (AFm-MoO_4) was synthesised from tricalcium aluminate (C_3A, i.e. $Ca_3Al_2O_6$), freshly prepared according to the method described by Mondal and Jeffery (1975) and Atkins et al. (1991), respectively, using different routes: i) by the suspension of C_3A and Na_2MoO_4 in deionised water and adjusting the pH with NaOH to pH 13.5 and curing for 2 months, ii) by suspending C_3A and $CaMoO_4$ in deionised water and adjusting the pH with KOH to pH 13.5 at room temperature and curing for 1 month, or iii) by suspending C_3A and $CaMoO_4$ in deionised water and curing for 1 month.

2.2 Preparation of HCP

HCP samples were prepared in a glove box under argon atmosphere from a commercially available Ordinary Portland cement (CEM I 32.5 R; Heidelberger Zement) using a water/cement ratio of 0.4 L kg^{-1}. After thorough mixing the paste was cast in cylindrical moulds. The monoliths were cured for at least 28 days submerged in water under anoxic conditions. The demoulded monoliths were subsequently stored at room temperature under argon atmosphere. The HCP was mechanically crushed for use in batch sorption experiments.

2.3 Phase characterization

Purity and structure of the synthesised hydration phases as well as the phase assemblage of the CEM I HCP were determined by X-ray diffraction analyses (XRD), employing a D4 Endeavor (Bruker AXS GmbH) with a θ-2θ geometry or alternatively a D8 Advance (Bruker AXS GmbH) with a θ-θ geometry, both equipped with Cu X-ray tubes, at tube power settings of 40 kV and 40 mA. The surface areas of the model phases and the crushed HCP were determined by multipoint N_2-BET measurements, employing a Quantachrome Autosorb 1; the Quantachrome AS1Win (v. 2.11) software was used for data treatment. Microstructural investigations of the synthesised phases and HCP were carried out by scanning electron microscopy (SEM) using a FEI Quanta 200F equipped with a field emission cathode. Energy-dispersive X-ray spectroscopy (EDX) was performed using an Apollo X Silicon Drift Detector (SDD) from EDAX. The SEM/EDX analyses were performed in low vacuum mode (60 Pa) to avoid coating the materials with gold or carbon. A detailed characterisation of the hydration phases and the HCP is provided in Lange et al. (2018) and Lange (2019), respectively. The

specific surface areas of the hydration phases are specified in Table S1 in the Supplementary Material.

Transmission electron microscopy (TEM), selected area electron diffraction (SAED) and EDX were performed on a FEI Technai G2 F20 transmission electron microscope operated at 200 kV accelerating voltage with a total beam current of about 2 nA (Ernst-Ruska-Centre for Microscopy and Spectroscopy with Electrons, 2016). The samples, present in the form of crystallites a few micrometres in size, were supported by a hexagonal copper grid for analysis. TEM images and SAED patterns were recorded from parts of the crystallites exposed over the free grid space with the incident electron beam perpendicular to the platelet normal. EDX spectra were recorded with the samples tilted by 15° towards the spectrometer. The EDX spectra were analysed with the TEM Image & Analysis software (FEI Company, The Netherlands) using the standard-less quantification method of Cliff and Lorimer (1975), based on k-factors and detector efficiencies tabulated in the software. Empirical Bremsstrahlung or multi-polynomial background subtraction was applied, depending on which provided a better fit to the spectral data away from the present emission lines. Due to this somewhat subjective background modelling approach and the large residual background intensities at the O-K and the Al-K lines, the relative error of the composition analysis was estimated to be about 10%.

2.4 Batch sorption experiments

Sorption distribution ratios (R_d values) and molybdate uptake kinetics were determined in static batch experiments under anoxic conditions. The sorption experiments with the single phases were performed in 20 mL LDPE bottles at solid-to-liquid (*S/L*) ratios between 0.005 kg L^{-1} and 0.04 kg L^{-1}, depending on the type and aim of the experiment. In the first set of experiments, solutions equilibrated with the respective hydration phases were used. For this purpose, the dried solids were equilibrated with deionized water (18.2 MΩ) for 14 days under anoxic conditions; solid and liquid phases were subsequently separated by filtration. The solids from the pre-equilibration step were discarded and fresh solids were used in the sorption experiments. The pH of the equilibrium solutions (ES) is provided in Table S2 in the Supplementary Material. Moreover, experiments were performed with artificial alkali-rich young cementitious water (ACW, pH >13) and a solution saturated with respect to portlandite (CH, pH ~12.5) to emulate conditions representative of concrete degradation

173 stages I and II (*e.g.*, Glasser, 2011; Hoch et al., 2012; Ochs et al., 2016). The ACW solution
174 was prepared from highly concentrated NaOH and KOH stock solutions subsequently
175 saturated with $Ca(OH)_2$ according to the method of Wieland et al. (1998). The final ACW
176 solution had a pH of 13.3, containing 0.114 mol L^{-1} Na and 0.18 mol L^{-1} K. The saturated
177 portlandite solution (CH) had a pH of 12.3 and contained 0.20 mol L^{-1} Ca.

178 For the sorption experiments, defined amounts of the respective solids were added to
179 the solutions and stored for 14 days, before molybdate was added in the form of Na_2MoO_4
180 at initial molybdate concentrations between $5 \cdot 10^{-6}$ and $1 \cdot 10^{-7}$ mol L^{-1} to avoid solution
181 supersaturation with respect to powellite. The molybdate concentration and pH of the
182 solutions were monitored for up to 60 days to ensure that steady state had been reached;
183 the bottles were shaken by hand regularly. To avoid the removal of solution due to sampling,
184 a separate test batch was used for each time step in the experiments addressing the uptake
185 kinetics. The timeframe required for experiments to determine the steady state R_d values
186 (duration 30 days) was then defined based on the results of the kinetic experiments. Prior to
187 analysis of the molybdate concentration in solution at the end of the sorption experiments,
188 liquid and solid phases were separated by filtration using USY-1 ultrafilters (10,000 Da,
189 Advantec). The sorption of molybdate to the LDPE bottles and filters was tested prior to the
190 sorption experiments and was found to be negligible. The remaining Mo concentrations in
191 solution were determined by inductively coupled plasma mass spectrometry (ICP-MS; Elan
192 6100 DRC, Perkin Elmer) and inductively coupled plasma optical emission spectrometry (ICP-
193 OES; Thermo Scientific iCAP7600) after acidification with HNO_3.The dilution factors as well as
194 the limits of detection (LOD) were determined individually for all the sample batches in
195 screening measurements to ensure measureable Mo concentrations. Typical values for the
196 LOD of both methods were in the order of 10^{-8} mol L^{-1} or less.

197 Sorption experiments with crushed HCP CEM I were performed in a similar fashion to the
198 experiments with the model hydration phases, using solutions that were equilibrated for 14
199 days with the crushed HCP. In these sorption experiments, lasting for 60 days, a solid-to-
200 liquid ratio of 0.005 kg L^{-1} was used, corresponding to a ratio of surface area to solution
201 volume of 120 m^2 L^{-1}.

The uptake of molybdate by the solids is described in terms of a distribution ratio R_d that is defined as the ratio between the amount of molybdate sorbed to the respective solid ($MoO_4^{2-}{}_{sorbed}$) and the concentration of molybdate remaining in the liquid phase ($MoO_4^{2-}{}_{solution}$) as

$$R_d = \frac{MoO_4^{2-}{}_{sorbed}}{MoO_4^{2-}{}_{solution}} \quad (1)$$

and calculated according to

$$R_d = \frac{MoO_4^{2-}{}_{ini} - MoO_4^{2-}{}_{t}}{MoO_4^{2-}{}_{t}} \frac{V}{m} \quad (2)$$

where $MoO_4^{2-}{}_{ini}$ is the initial molybdate concentration in solution, and $MoO_4^{2-}{}_{t}$ the concentration at time *t*, respectively, *V* is the volume of the liquid phase, and *m* the mass of solid phase used in the experiment. Uncertainties in the R_d values were estimated based on the propagated uncertainties associated with the experimental design and those resulting from the chemical analysis, and are included in the respective tables and figures.

2.5 Thermodynamic modelling

To aid in the setting up and interpreting the batch sorption experiments, the aqueous speciation of the components in solution and saturation indices of relevant phases were calculated, employing the geochemical code PhreeqC Ver. 3.4.0 (Parkhurst and Appelo, 2013). The ANDRA ThermoChimie v.9b thermodynamic database (Consortium Andra – Ondraf/Niras – RWM; Giffaut et al., 2014; Grivé et al., 2015), which includes data on cement hydration phases from Blanc et al. (2010a,b), was used for the thermodynamic modelling. The activities of aqueous species were calculated using the specific ion interaction (SIT) approach (*cf.* Brønsted, 1922; Guggenheim, 1935; Scatchard, 1936). Table S3 in the Supplementary Material provides information on the powellite saturation state in the experiments performed to determine the steady state R_d values.

3. Results and discussion

3.1 Molybdate uptake by single hydration phases

The kinetics of the molybdate uptake by the various model hydration phases was determined at a *S/L*-ratio of 0.005 kg L^{-1} for up to 60 days. The results of the sorption tests as

a function of time are shown in Fig. 2. A steady state was generally reached after 30 days at the latest. The solution pH was constant over the time of the experiments. The most pronounced uptake was observed for hydrogarnet.

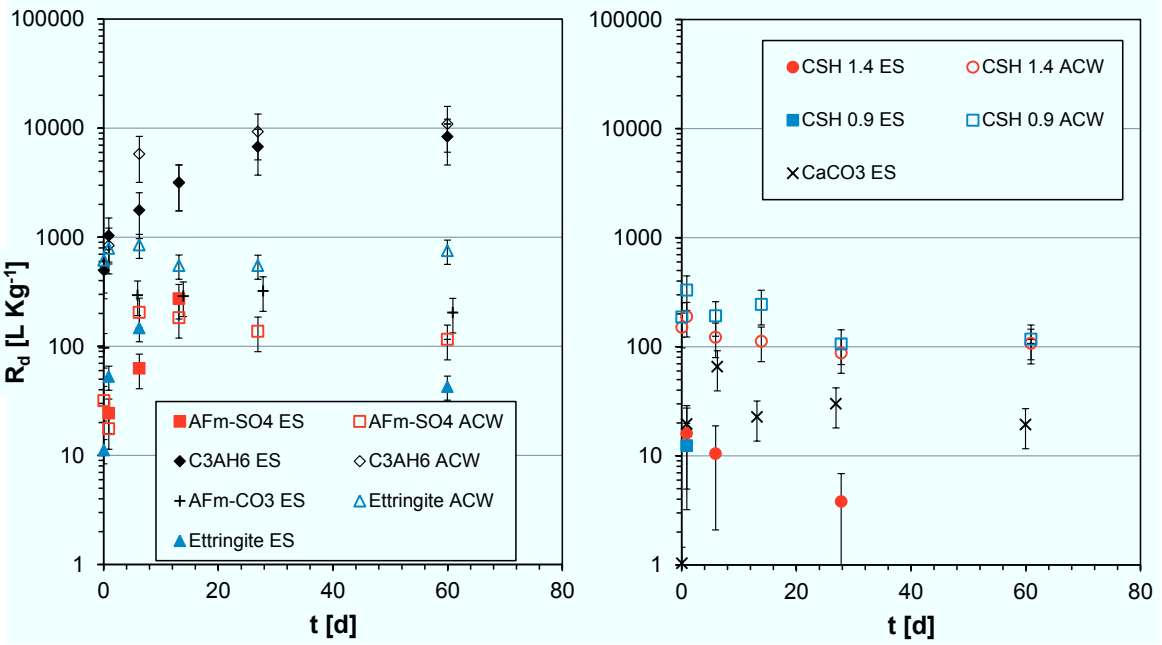

Fig. 2. Kinetics of the molybdate uptake by various model hydration phases in different solutions (ES: equilibrium solution; ACW: artificial young cement water (pH 13.3); C_3AH_6: hydrogarnet).

The steady state R_d values for the molybdate uptake in the different systems determined at *S/L*-ratios of 0.04 L kg^{-1} are summarised in Table 1 and shown in Fig. S1 in the Supplementary Material. The uptake of MoO_4^{2-} by C-S-H in equilibrium solutions was found to increase with increasing Ca/Si ratio from $R_d \approx 430$ L kg^{-1} for C-S-H 0.9 to $R_d \approx 750$ L kg^{-1} for C-S-H 1.4. This trend, in line with the increasingly positive surface charge of C-S-H at Ca/Si ratios > 1.2, indicates that the molybdate uptake by C-S-H is mainly due to electrostatic sorption. Distinctly lower R_d values were observed in alkali-rich young cementitious water, which might be due to competition with OH^- ions for sorption sites, suggesting lower molybdate sorption and retention by C-S-H in young alkali-rich cementitious systems. The results show that C-S-H phases in cementitious materials can play an important role with respect to the retention of molybdenum, in particular in aged systems with lower alkali concentrations in the pore water (degradation stages II and III).

Table 1

Distribution coefficients R_d for molybdate uptake by cement hydration phases in different solutions (ES: equilibrium solution; ACW: artificial young cement water (pH 13.3), CH: saturated portlandite solution (pH 12.3), duration of the experiments: 30 days).

Phase	R_d [L kg^{-1}]		
	ES	ACW	CH
C-S-H 0.9	432 ± 26	143 ± 9	
C-S-H 1.4	781 ± 41	98 ± 5	
AFm-SO_4	1,571 ± 115	55 ± 2	240 ± 220
AFm-CO_3	1,564 ± 90		535 ± 481
Ettringite	122 ± 4	122 ± 4	23 ± 21
Hydrogarnet C_3AH_6	3,037 ± 436	1,909 ± 142	594 ± 436
Portlandite	789 ± 28		44 ± 28
Calcite	321 ± 18		3 ± 2

As expected, a pronounced molybdate uptake (R_d ≈ 1,550 L kg^{-1} in equilibrium solution) by both AFm-SO_4 and AFm-CO_3 was observed, indicating no preference of the uptake with respect to the nature of the interlayer anion (i.e. planar CO_3 or tetrahedral SO_4). However, the uptake of molybdate was found to be distinctively lower in saturated portlandite solution and in particular in artificial young cementitious pore water. One mode of molybdate uptake in AFm is anion exchange in the interlayer of the LDH structure (*cf*. Kindness et al., 1994; Ma et al. 2017; Marty et al., 2018). XRD studies on AFm-SO_4 used in the batch sorption experiments showed an increase in the basal spacing compared to pure AFm-SO_4, suggesting a structural incorporation of MoO_4^{2-} ions in the AFm structure by anion exchange with the interlayer anion, since the size of the molybdate oxo-anions (Mo-O bond length ~1.77 Å) is larger than that of the sulphate ions (S-O bond length ~1.47 Å) (*cf*. Hawthorne et al., 2000). However, the increase in the basal spacing might also be attributed to an increasing number of water molecules in the interlayer in the Mo-substituted AFm-SO_4. Recent XRD, X-ray absorption spectroscopy (XAS), and TEM/SAED investigations by Ma et al. (2017) on the sorption of molybdate by AFm-SO_4 and AFm-Cl_2 showed that, with increasing molybdate concentration in solution and surface coverage on the AFm, the MoO_4^{2-} uptake can be interpreted by three retention mechanisms, i.e. formation of edge sites complexes, interlayer anion exchange, and finally $CaMoO_4$ precipitation. Marty et al. (2018) found in their study that molybdate was exchanged for two chloride anions in the

interlayer mid-plane of AFm-Cl_2 and that the competition between molybdate and OH^- leads to a decrease in molybdate sorption with increasing pH, as also observed in our study for AFm-SO_4.

Ettringite is known for its ability to incorporate various monovalent and bivalent oxo-anions by solid-solution formation due to exchange for the sulphate groups (*cf*. Myneni et al. 1998; Ochs et al., 2002, 2016; Zhang, 2000; Zhang and Reardon, 2003) and showed a lower tendency to incorporate molybdate compared to the AFm phases (R_d ≈ 120 L kg^{-1} in equilibrium solution) in agreement with the findings of Kindness et al. (1994). According to Zhang and Reardon (2003), ettringite shows a preference for SeO_4^{2-} over MoO_4^{2-} incorporation. Sorption experiments with artificial young cement waters at pH 13.3 revealed higher R_d values than those obtained using alkali-free portlandite saturated solutions at pH 12.3, indicating a stronger retention of molybdate by ettringite in young cementitious systems compared to the later degradation stages. The observed retention of molybdate by portlandite (R_d ≈ 790 L kg^{-1}) might be attributable to the formation of $CaMoO_4$ precipitates or clusters on the portlandite surface, although the bulk solution was undersaturated with respect to powellite in the experiment (saturation index $SI_{powellite}$ = -0.73). However, no discernible powellite crystallites or spots of local Mo enrichment were observed in SEM/EDX investigations of the portlandite surface after the sorption experiment.

Off all the hydration phases investigated, the highest molybdate uptake was observed for hydrogarnet (R_d value ≈ 3,000 L kg^{-1} in equilibrium solution). The uptake was found to be higher in more alkaline young cementitious waters compared to the portlandite saturated solution representing aged cementitious systems. To obtain further insights into the uptake mechanism, the solids used in the sorption batch experiments were subsequently studied by XRD and SEM. However, no changes in the XRD patterns of the solids as consequence of the Mo-uptake were observed. Moreover, no Mo could be detected by EDX on the surface of the hydrogarnet, probably due to the detection limits of the EDX. However, the initially well-crystallised and idiomorphic hydrogarnet crystals (*cf*. Fig. 3a), revealed distinct dissolution features after the sorption experiments (*cf*. Fig. 3b). Additionally, in some of the solids employed in the sorption experiments performed in ACW, newly formed small (diameter ~5 µm) sheet-like crystals with (pseudo)hexagonal habitus were observed (*cf*. Fig. 3c). These rare crystals contain measurable quantities of Mo, Ca and Al, suggesting the formation of an

AFm-MoO_4 phase. These results indicate that the uptake of molybdate in systems with hydrogarnet is probably due to partial dissolution of hydrogarnet and the precipitation of small amounts of an AFm-like molybdate phase.

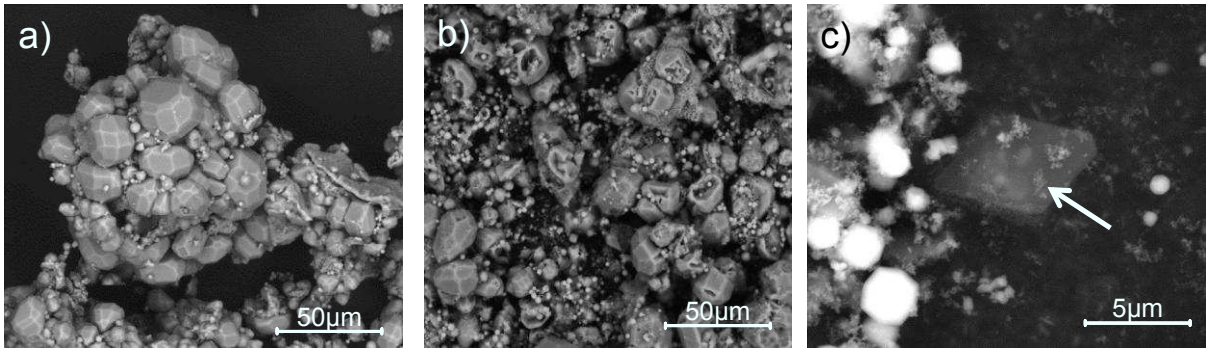

Fig. 3. SEM images of hydrogarnet before (a) and after (b) uptake experiments with molybdate, showing the formation of (pseudo)hexagonal secondary phases (c), indicated by the arrow.

However, the amounts of this Mo-bearing phase newly formed in the batch sorption experiments at an initial MoO_4^{2-} concentration of 10^{-6} mol L^{-1} were too low for further investigations. Therefore, in additional sorption experiments, the MoO_4^{2-} concentration was increased up to 10^{-3} mol L^{-1} until the precipitated phase contributed to the XRD pattern obtained after the end of the sorption experiment (*cf*. Figure S2 in the Supplementary Material). The interlayer spacing of the newly formed phase was found to be 8.59 Å (d_{003}) and 4.29 Å (d_{006}), respectively, in good agreement with the literature data for AFm-MoO_4 from Kindness et al. (1994) and Marty et al. (2018), further supporting the precipitation of AFm-MoO_4 as a retention mechanism in the molybdate-hydrogarnet system. No powellite precipitation was discernible in the diffraction patterns. However, additional reflexes at 11.7° 2Θ corresponding to d_{003} of AFm-CO_3 could be attributed to carbonation during sample preparation, drying and measurement. Kindness et al. (1994) reported a interlayer spacing of 8.70 Å (d_{003}) and 4.32 Å (d_{006}) for AFm-MoO_4 comprising eight H_2O molecules in the interlayer. A similar interlayer distance d_{003} of 8.60 Å was reported by Marty et al. (2018) for a chloride-bearing AFm, where the Cl ions in the interlayer were partially substituted by molybdate. In contrast, Ma et al. (2017) determined interlayer distances (d_{003}) of 10.3 Å and 10.4 Å, respectively, for AFm-Cl_2 and AFm-SO_4 partially substituted by molybdate. The interlayer distances of the AFm phases are strongly dependent on the state of hydration,

thus the different interlayer spacing determined by Ma et al. (2017) can probably be attributed to a larger amount of water in the interlayer, which can also be influenced by the drying procedures. In a further uptake experiment with C_3AH_6 performed again at an initial MoO_4^{2-} concentration of 10^{-3} mol L^{-1}, but using a prolonged reaction time, a decrease of the aqueous molybdate concentration to less than 10^{-6} mol L^{-1} was observed after a reaction time of two months. Here, EDX spot measurements performed after termination of the experiment revealed the presence of Mo in the (pseudo) hexagonal AFm-like crystals, whereas no Mo was found at the surface of the hydrogarnet (*cf*. Fig. 4).

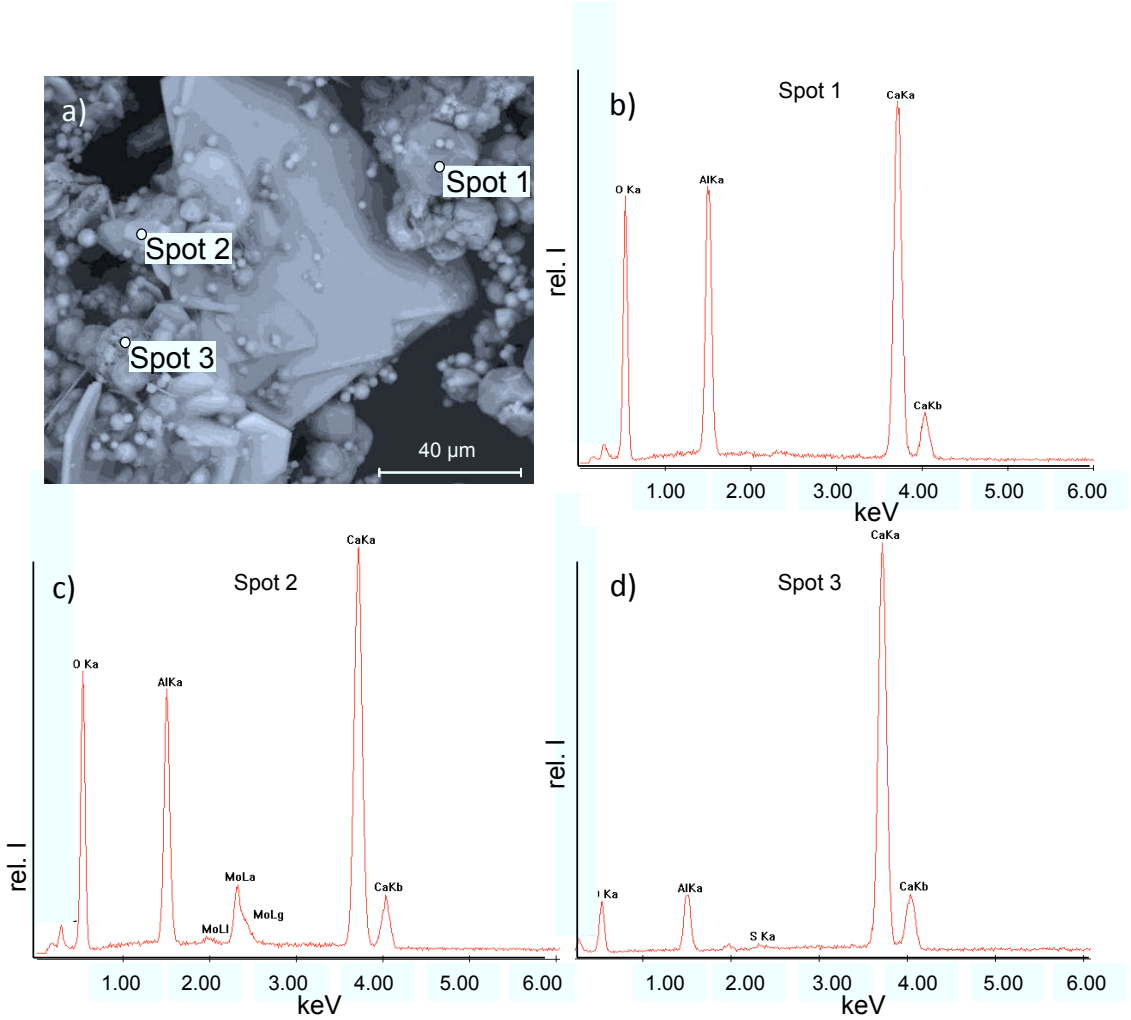

Fig. 4. a) SEM image of C_3AH_6 after 2 months reaction with a solution initially containing 10^{-3} mol L^{-1} MoO_4^{2-} showing the formation of AFm platelets, b) and d) EDX spectrum of hydrogarnet (spot 1 and spot 3), and c) EDX spectrum of AFm platelet, indicating the formation of a AFm molybdate phase (spot 2).

3.2 Characterisation of molybdate-bearing phases formed under highly alkaline conditions

To gain additional insights into the nature of molybdate-bearing AFm-like phases that may form as secondary phase under highly alkaline cementitious conditions, specific synthesis routes were used to obtain the phases in sodium, potassium or calcium rich solutions (*cf.* Section 2.1). Fig. 5 shows SEM images and XRD patterns of the molybdate-bearing AFm phases synthesised either in alkaline sodium- or potassium-rich solutions.

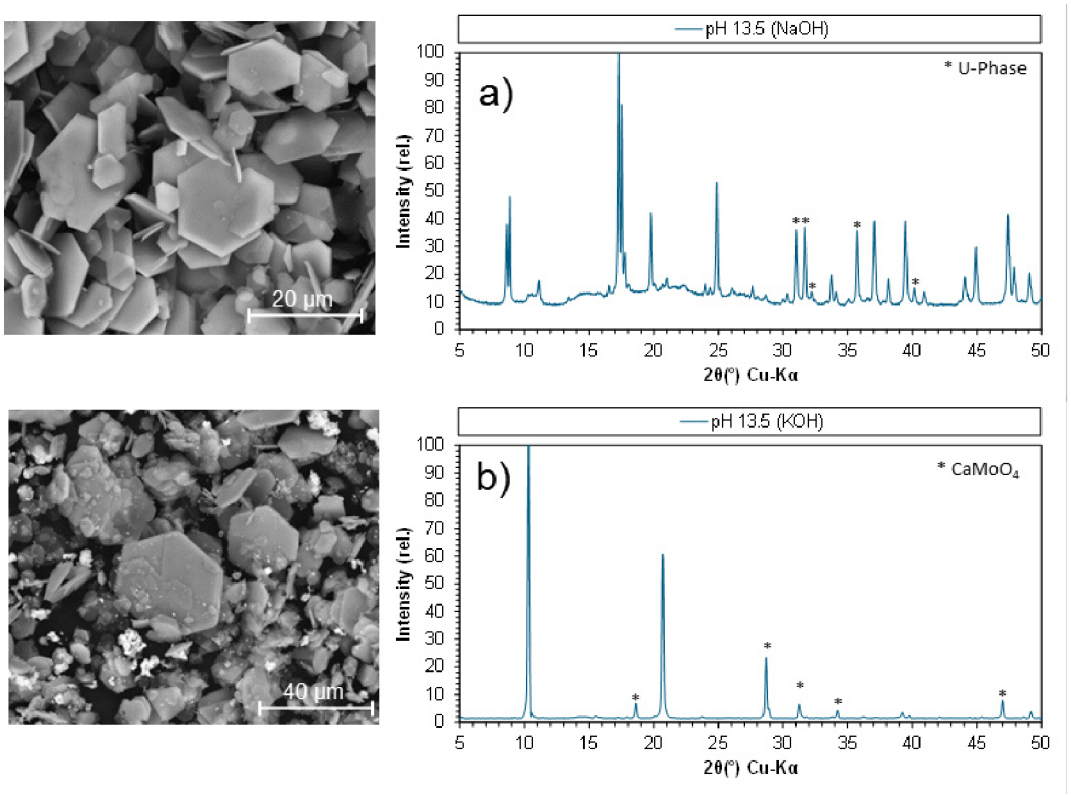

Fig. 5. a) SEM image and XRD pattern of AFm-MoO_4 synthesised in Na-rich alkaline conditions (final pH = 12.9) (reflexes marked with an asterisk potentially originate from an molybdate-analogue of the U-phase), and b) SEM image and XRD pattern of AFm-MoO_4 synthesised in K-rich alkaline conditions (final pH = 13.5) (reflexes marked with an asterisk originate from powellite impurities).

The product obtained in the sodium-bearing system at a final pH of 12.9 was well crystallised and had a sheet-like appearance similar to AFm (Fig 5a). SEM/EDX measurements revealed a stoichiometric composition of Ca:Al:Mo of 4:2:1, in accordance with the AFm composition $Ca_4Al_2(OH)_{12}(MoO_4)\cdot nH_2O$. The peak splitting of the d_{003} and d_{006} reflexes in the XRD pattern indicates two different hydration states of the interlayer anions. The reflexes of AFm-MoO_4 at 8.58 °2Θ and 17.26 °2Θ corresponding to interlayer distances of 10.3 Å (d_{003}) and 5.13 Å (d_{006}), respectively, are similar to those observed by Kindness et al. (1994) for molybdate-bearing AFm with four water molecules in the interlayer and the

362 interlayer distance observed by Ma et al. (2017) in partially molybdate-substituted AFm-SO_4
363 and AFm-Cl_2. However, it has to be noted that the interlayer distances reported in Kindness
364 et al. (1994) for the phase with the lower water content (reported as
365 $Ca_3Al_2O_6{\cdot}CaMoO_4{\cdot}10H_2O$) were larger than for the phase with the higher water content
366 (reported as $Ca_3Al_2O_6{\cdot}CaMoO_4{\cdot}14H_2O$). According to Kindness et al. (1994), the X-ray pattern
367 of the former resembled a typical AFm pattern, whereas that of the latter more closely
368 resembled the pattern of $Ca_4Al_2O_7{\cdot}19H_2O$ (i.e. $Ca_4Al_2(OH)_{12}(OH)_2\ 12H_2O$, the stable AFm-type
369 phase in the $CaO\text{-}Al_2O_3\text{-}H_2O$ system below 50 °C, *cf*. Stöber and Pöllmann, 2017).

370 The XRD pattern (Fig. 5a) showed some additional reflexes besides the well-known basal
371 reflex patterns of AFm-type structures. It has to be noted that the (undried) product had
372 been mixed with cork flour during preparation of the XRD specimen to avoid a preferred
373 orientation of the AFm platelets and the consequent obfuscation of reflexes of minor phases
374 (or AFm-related reflexes at higher 2Θ values) due to the high intensities of the basal
375 reflexes. The additional reflexes in Fig. 5a that cannot be attributed to AFm-MoO_4 reveal
376 similarities to the reflex pattern of the U-phase ($4CaO{\cdot}0.9Al_2O_3{\cdot}1.1SO_3{\cdot}0.5Na_2O{\cdot}16H_2O$). This
377 phase, a sodium substituted AFm phase that can form, for example, by the reaction of C_3A
378 with sodium-sulphate-rich solutions or in cemented sulphate-rich wastes (*cf*. Li et al., 1996;
379 Li and Le Bescop, 1997) was first described by Dosch and Zur Strassen (1967). Li et al. (1996;
380 1997) investigated this phase and its formation in cementitious systems with respect to
381 potential deleterious expansive effects. They presumed a hexagonal or pseudo-hexagonal
382 layered structure for the U-phase with similarities to AFm and a similar habitus (*i.e.*
383 (pseudo)hexagonal platelets). The pattern of the XRD reflexes not associated with AFm in
384 Fig. 5a and the synthesis route for this material employing C_3A in sodium rich, highly alkaline
385 conditions suggests the formation of a molybdate analogue to the U-phase as an impurity in
386 the synthesis of the AFm. However, it has to be noted that several reflexes of the U phase
387 coincide with those of molybdate AFm so that the identification of small amounts of a
388 molybdate bearing U-phase by means of XRD is somewhat ambiguous. In the K-rich system
389 (Fig. 5b), as well as in the alkali-free system, only some powellite impurities were observed
390 besides the AFm-MoO_4. SEM investigations on the microstructure of the material obtained in
391 the K-rich system revealed again the generally high crystallinity of the hexagonal sheet-like
392 AFm-MoO_4, exceeding a crystal size of 20 µm (Fig 5b). The XRD reflexes of this AFm-MoO_4 at
393 10.32 °2Θ and 20.74 °2Θ correspond to interlayer distances of 8.56 Å (d_{003}) and 4.28 Å (d_{006}),

394 respectively, suggesting a lower amount of water molecules in the interlayer compared to
395 the AFm-MoO_4 synthesised in the Na-bearing system. The XRD pattern of the AFm-MoO_4
396 from the alkali-free synthesis route, formed at lower pH (final pH = 12.1), was found to be
397 rather similar to that in the K-bearing system (*cf*. Fig. S3 in the Supplementary Material),
398 containing, however, slightly higher amounts of powellite impurities.

399 A TEM study was performed for a more detailed investigation of the phases present in
400 the sodium-rich system. The TEM images revealed the generally (pseudo)hexagonal, platy
401 habitus of all phases with a size of about 5 to 10 µm (*cf*. Fig. 6), besides traces of powellite
402 impurities, one of the educts in the synthesis. However, despite the similarities of all the
403 platelets with respect to their morphology, distinct differences in the electron diffraction
404 patterns were observed. The electron diffraction patterns were generally obtained along the
405 001 zone axis, due to the preferred orientation of the platelets. The majority of the platelets
406 exhibited a hexagonal or trigonal symmetry (lattice parameters $a = b$, $\gamma = 120°$) with a lattice
407 constant $a = 5.71 \pm 0.06$ Å (Fig. 6, left), and were assigned to the AFm-MoO_4 phase. In a few
408 cases, platelets with a triclinic or monoclinic symmetry occurred (Fig. 6, centre) that
409 exhibited slightly smaller lattice constants ($a \approx 5.5$ Å, $b \approx 5.1$ Å). However, due to the scarcity
410 of these platelets, no discrete values for the lattice constants of this phase could be
411 obtained. Moreover, some trigonal platelets were found to overlap with a slight rotation.
412 Here, the SAED patterns showed additional weak satellite spots between the primary
413 reflexes, indicating the presence of lattice disorder, potentially related to the oxygen
414 sublattice (Fig. 6, right). The EDX spectra generally revealed Ca/Al ratios of about 2,
415 indicative of either a molybdate AFm or a molybdate-bearing U-phase, and the presence of
416 Mo. In some spectra, the presence of small amounts of Na was indicated. However, due to
417 the strong overlap with the Cu-L lines (from the TEM sample grid), a quantification was not
418 possible.

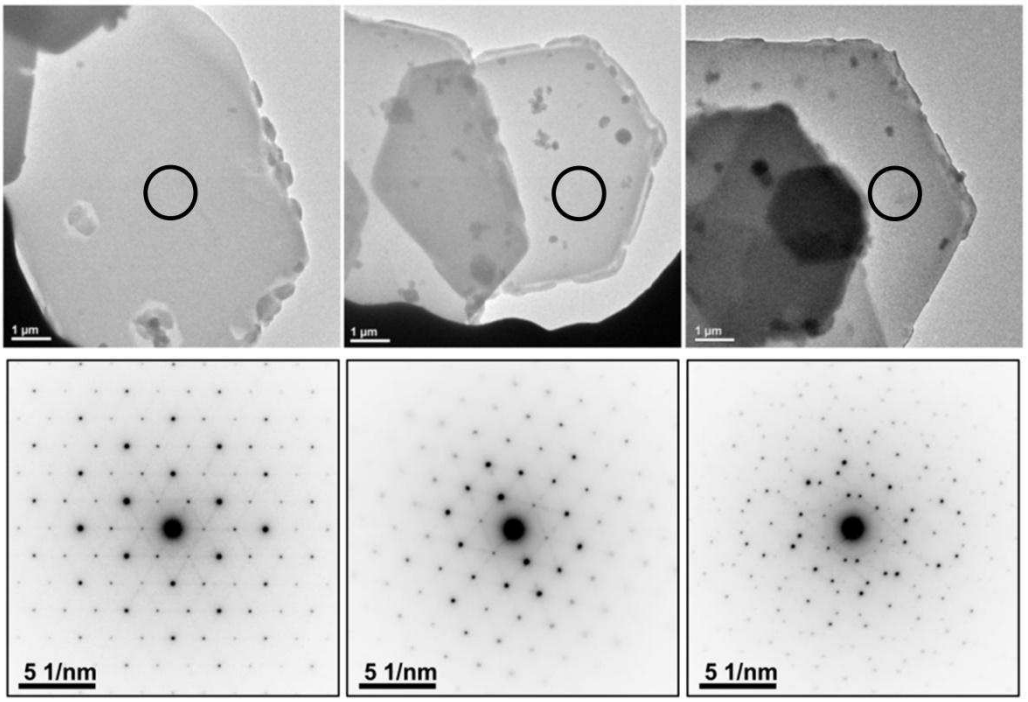

Fig. 6. TEM images and electron diffraction patterns of AFm-like phases: AFm-MoO_4 (left), a lower-symmetric molybdate-bearing phase, potentially a U phase analogue (centre), and overlay pattern of rotated trigonal platelets with satellite reflexes (right), indicating the presence of lattice disorder (the circles mark the locations of the SAED patterns).

The TEM study confirmed that the synthesised material comprised a mixture of AFm-MoO_4 and another chemically and structurally closely related Mo-bearing phase, which is suggested to be a molybdate analogue of the U-phase. Moreover, the results of the TEM study indicate a lower symmetry (*i.e.* triclinic or monoclinic) of the Mo-analogue of the U-phase compared to AFm, which could indicate that also the sulphate-bearing U-phase has a pseudo-hexagonal rather than a hexagonal structure (*cf*. Li et al., 1996, 1997).

3.3 Molybdate uptake by HCP

The results of the sorption tests using crushed HCP are shown in Fig. 7. The uptake of molybdate by the CEM I HCP reached a steady-state R_d value of about 300 L kg^{-1} after 8 days. The pH in the solution remained constant throughout the sorption experiment at pH 12.6. Due to the low *S/L*-ratio used in the experiments and the low inventory of alkalis in the system, the experiment refers to a slightly degraded cementitious material in stage II (*cf*. Tits et al., 2006). The measured distribution ratios for the uptake of molybdate by CEM I HCP are

in good agreement with the literature data on molybdate sorption by OPC from Kato et al. (2002). However, the R_d values are distinctly higher than the data for selenate sorption on CEM I compiled in Ochs et al. (2016) and the recommended values for selenate sorption in the different cement degradation stages. This suggests that the applicability of selenate sorption parameters for deriving the molybdate retention properties of cementitious materials is limited. The results obtained for molybdate retention in the HCP system are in qualitative agreement with the uptake behaviour observed for the single phases, taking into account the pH in the experiment and the lower accessible surface area in the crushed HCP. Based on the single-phase study, not only AFm but also the C-S-H phases contribute to molybdenum retention.

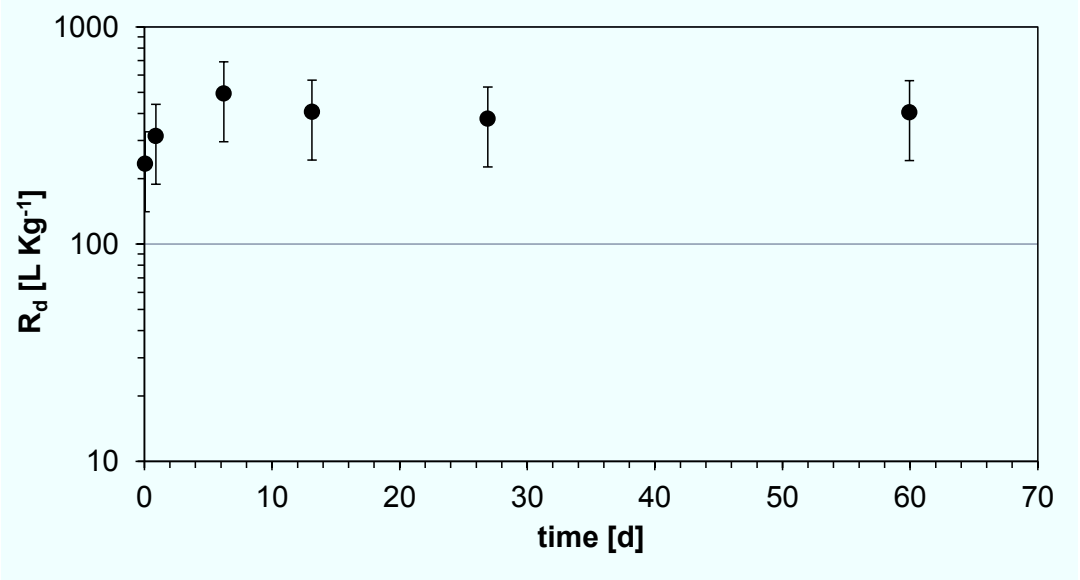

Fig. 7. Uptake kinetics of MoO_4^{-2} by HPC made from CEM I.

4. Conclusions

In this study, the uptake of molybdate by various cement hydration phases and HCP was investigated in a bottom-up approach. Batch experiments on individual phases present in hydrated OPC and blended cements confirmed the important role of AFm with respect to molybdate retention in cementitious systems, in particular due to anion exchange in the interlayer. Moreover, a distinct contribution of the C-S-H phases to Mo retention in cementitious systems was observed, which can be attributed to electrostatic sorption. As an additional retention mechanism, the neo-formation of a molybdate-bearing AFm in systems

with hydrogarnet was identified. In addition, the results indicate that in sodium-rich systems, besides AFm-MoO_4 and powellite, the formation of an analogue of the U-phase might contribute to the retention of molybdate, whereas in potassium-dominated systems and also in alkaline calcium-bearing solutions (*e.g.*, in cementitious pore waters in the portlandite stage) only AFm-MoO_4 forms in addition to powellite that may be present.

The findings have implications when selecting cementitious grouts and/or backfill materials for radioactive waste streams containing Mo-93 and enhance the sparse data currently available on molybdate retention in cementitious materials (*cf*. Ochs et al., 2016). The approach pursued in this study improved the understanding of the contributions of individual hydration phases to the overall retention of Mo in cementitious materials and the respective uptake mechanisms. The distribution ratios obtained for the main hydration phases under specific pore water conditions representing different degradation stages of cementitious materials could be used as a basis for a component additive approach to provide an envelope of the retention properties of complex cement-based materials (*e.g.*, backfill mortar or structural concrete) for Mo-93 in a deep geological repository or a near-surface disposal facility. In addition to safety assessments for the disposal of radioactive wastes, the data can also be employed in models used for the evaluation of clearance or disposal options for contaminated and/or activated building materials and rubble arising during the dismantling of nuclear facilities (*cf*. Bath et al., 2004; Deissmann et al., 2005). Moreover, the results suggests that cementitious materials with high AFm content and C-S-H with high Ca/Si ratios would be beneficial for the solidification of specific Mo-93-bearing waste streams in terms of enhanced sorption properties for molybdate.

Acknowledgements

The research leading to these results has received funding from the European Union's Horizon 2020 Research and Innovation Programme under grant agreement no 662147 (Cebama).

References

Aimoz, L., Wieland, E., Taviot-Gueho, C., Dahn, R., Vespa, M., Churakov, S.V., 2012. Structural insight into iodide uptake by AFm phases. Environ. Sci. Technol. 46, 3874-3881.

489 Atkins, M., Glasser, F.P., 1992. Application of Portland cement-based materials to radioactive
490 waste immobilization. Waste Manag. 12, 105-131.

491 Atkins, M., Macphee, D., Kindness, A., Glasser, F.P., 1991. Solubility properties of ternary and
492 quaternary compounds in the calcia-alumina-sulfur trioxide-water system. Cem. Concr. Res.
493 21, 991-998.

494 Atkins, M., Glasser, F.P., Kindness, A., 1992. Cement hydrate phases: solubility at 25°C. Cem.
495 Concr. Res. 22, 241-246.

496 Bath, A., Deissmann, G., Jefferis, S., 2003. Radioactive contamination of concrete: Uptake
497 and release of radionuclides. ASME 2003: The 9th International Conference on Radioactive
498 Waste Management and Environmental Remediation, https://doi.org/10.1115/ICEM2003-
499 4814.

500 Baur, I., Keller, P., Mavrocordatos, D., Wehrli, B., Johnson, C.A., 2004. Dissolution-
501 precipitation behaviour of ettringite, monosulfate, and calcium silicate hydrate. Cem. Concr.
502 Res. 34, 341-348.

503 Beattie, T.M., Williams, S.J., 2012. An overview of near-field evolution research in support of
504 the UK geological disposal programme. Mineral. Mag. 76, 2995-3001.

505 Bel, J.P., Wickham, S.M., Gens, R.M.F., 2006. Development of the supercontainer design for
506 deep geological disposal of high-level heat emitting radioactive waste in Belgium. Mater.
507 Res. Soc. Symp. Proc. 932.

508 Berner, U.R., 1992. Evolution of pore water chemistry during degradation of cement in a
509 radioactive waste repository environment, Waste Manag. 12, 201-219.

510 Blanc, P., Bourbon, X., Lassin, A., Gaucher, E.C., 2010a. Chemical model for cement based
511 materials: Temperature dependence of thermodynamic functions for nanocrystalline and
512 crystalline C–S–H phases. Cem. Concr. Res. 40, 851-866.

513 Blanc, P., Bourbon, X., Lassin, A., Gaucher, E.C., 2010b. Chemical model for cement based
514 materials: thermodynamic data assessment for phases other than C–S–H. Cem. Concr. Res.
515 40, 1360-1374.

516 Brown, D.A., Chadwick, M.B., Capote, R., Kahler, A.C., Trkov, A., Herman, M.W., Sonzogni,
517 A.A., Danon, Y., Carlson, A.D., Dunn, M., Smith, D.L., Hale, G.M., Arbanas, G., Arcilla, R.,
518 Bates, C.R., Beck, B., Becker, B., Brown, F., Casperson, R.J., Conlin, J., Cullen, D.E., Descalle,
519 M.-A., Firestone, R., Gaines, T. , Guber, K.H., Hawari, A.I., Holmes, J., Johnson, T. D., Kawano,
520 T., Kiedrowski, B.C., Koning, A.J., Kopecky, S., Leal, L., Lestone, J.P., Lubitz, C., Marquez
521 Damian, J.I., Mattoon, C.M., McCutchan, E.A., Mughabghab, S., Navratil, P., Neudecker, D.,
522 Nobre, G.P.A., Noguere, G., Paris, M., Pigni, M.T., Plompen, A.J., Pritychenko, B., Pronyaev,
523 V.G., Roubtsov, D., Rochman, D., Romano, P., Schillebeeckx, P., Simakov, S., Sin, M., Sirakov,
524 I., Sleaford, B., Sobes, V., Soukhovitskii, E.S., Stetcu, I., Talou, P., Thompson, I., van der
525 Marck, S., Welser-Sherrill, L., Wiarda, D., White, M., Wormald, J. L., Wright, R.Q., Zerkle, M.,
526 Zerovnik, G., Zhu, Y., 2018. ENDF/B-VIII.0: The 8th major release of the Nuclear Reaction

527 Data Library with CIELO-project cross sections, new standards and thermal scattering data.
528 Nucl. Data Sheets 148, 1-142.

529 Brønsted, J.N., 1922. Studies of solubility: IV. The principle of specific interaction of ions. J.
530 Am. Chem. Soc. 44, 877-898.

531 Cliff, G., Lorimer, G.W., 1975. The quantitative analysis of thin specimens. J. Mirosc. 103,
532 203-207.

533 Deissmann, G., Bath, A., Jefferis, S., Thierfeldt, S., Wörlen, S., 2006. Development and
534 application of knowledge-based source-term models for radionuclide mobilisation from
535 contaminated concrete. Mater. Res. Soc. Symp. Proc. 932, 259-266.

536 Dosch, W., Zur Strassen, H., 1967. Ein alkalihaltiges Calciumaluminatsulfathydrat (Natrium-
537 Monosulfat). Zement-Kalk-Gips 20, 392-401.

538 Drace, Z., Ojovan, M.I., 2013. A summary of IAEA coordinated research project on
539 cementitious materials for radioactive waste management, in: Bart, F., Cau-dit-Coumes, C.,
540 Frizon, F., Lorente, S. (eds): Cement-based materials for nuclear waste storage, Springer, 3-
541 11.

542 Ernst Ruska-Centre for Microscopy and Spectroscopy with Electrons, 2016. FEI Tecnai G2
543 F20. Journal of large-scale research facilities 2, A77. http://dx.doi.org10.17815/jlsrf-2-138.

544 Evans, N.D.M., 2008. Binding mechanisms of radionuclides to cement. Cem. Concr. Res. 38,
545 543-553.

546 Giffaut, E., Grivé, M., Blanc, Ph., Vieillard, Ph., Colàs, E., Gailhanou, H., Gaboreau, S., Marty,
547 N., Madé, B., Duro, L., 2014. Andra thermodynamic database for performance assessment:
548 ThermoChimie. Appl. Geochem. 49, 225-236.

549 Glasser, F.P., 1997. Fundamental aspects of cement solidification and stabilization. J. Hazard.
550 Mater. 52, 151-170.

551 Glasser, F.P., 2001. Mineralogical aspects of cement in radioactive waste disposal. Mineral.
552 Mag., 65, 621-633.

553 Glasser, F.P., 2002. Characterisation of the barrier performance of cements. Mat. Res. Soc.
554 Symp. Proc. 713, JJ9.1.

555 Glasser, F.P., 2011. Application of inorganic cements to the conditioning and immobilisation
556 of radioactive wastes. In: Ojovan, M.I. (ed.) Handbook of advanced radioactive waste
557 conditioning technologies, Woodhead, 67-135.

558 Gougar, M.L.D., Scheetz, B.E., Roy, D.M., 1996. Ettringite and C-S-H Portland cement phases
559 for waste ion immobilization: A review. Waste Manag. 16, 295-303.

560 Grambow, B., López-García, M., Olmeda, J., Grivé, M., Marty, N.C.M, Grangeon, S., Claret, F.,
561 Lange, S., Deissmann, G., Klinkenberg, M., Bosbach, D., Bucur, C., Florea, I., Dobrin, R., Isaacs,

562 M., Read, D., Kittnerová, J., Drtinová, B., Vopálka, D., Cevirim-Papaioannou, N., Ait-Mouheb,
563 N., Gaona, X., Altmaier, M., Nedyalkova, L., Lothenbach, B., Tits, J., Landesman, C.,
564 Rasamimanana, S., Ribet, S., 2020. Retention of radionuclides on cementitious systems: main
565 outcome of the CEBAMA project. Appl. Geochem. 112, 104480.

566 Grivé, M., Duro; L., Colàs, E., Giffaut, E., 2015. Thermodynamic data selection applied to
567 radionuclides and chemotoxic elements: An overview of the ThermoChimie-TDB. Appl.
568 Geochem. 55, 85-94.

569 Guggenheim, E.A., 1935. The specific thermodynamic properties of aqueous solutions of
570 strong electrolytes. Philos. Mag. 19, 588-643.

571 Harris, A.W., Manning, M.C., Tearle, W.M., Tweed, C.J., 2002. Testing of models of the
572 dissolution of cements - leaching of synthetic C-S-H gels. Cem. Concr. Res. 32, 731-746.

573 Hawthorne, F.C., Krivovichev, S.V., Burns, P.C., 2000. The crystal chemistry of sulfate
574 minerals. Rev. Mineral. 40, 1-112.

575 Heath, T.G., Illet, D.J., Tweed, C.J., 2000. Development of a near-field sorption model for a
576 cementitious repository. UK Nirex report AEAT/R/ENV/0229, 41 pp.

577 Hoch, A.R., Baston, G.M.N., Glasser, F.P., Hunter, F.M.I., Smith, V., 2012. Modelling evolution
578 in the near field of a cementitious repository. Mineral. Mag. 76, 3055-3069.

579 Holland, T.R., Lee, D.J., 1992. Radionuclide getters in cement. Cem. Concr. Res. 22, 247-258.

580 Jantzen, C., Johnson, A., Read, D., Stegemann, J., 2010. Cements in waste management. Adv.
581 Cem. Res. 22, 225-231.

582 Kato, H., Mine, T., Mihara, M., Ohi, T., Honda, A., 2002. The sorption database of
583 radionuclides for cementitious materials. Japan Atomic Energy Agency, JNC TN8400 2001-
584 029, 56 pp.

585 Kindness, A., Lachowski, E.E., Minocha, A.K., Glasser, F. P., 1994. Immobilization and fixation
586 of molybdenum (VI) by Portland cement. Waste Manag. 14, 97-102.

587 Lange, S., 2019. Structural uptake and retention of safety relevant radionuclides by
588 cementitious materials. PhD thesis, RWTH Aachen University.

589 Lange, S., Kowalski, P., Pšeničkа, M., Klinkenberg, M., Rohmen, S., Bosbach, D., Deissmann,
590 G., 2018. Uptake of ^{226}Ra in cementitious systems: A complementary solution chemistry and
591 atomistic simulation study. Appl. Geochem. 96, 204-216.

592 Li, G., Le Bescop, P., 1997. Degradation mechanisms of cement-stabilised wastes by internal
593 sulfate associated with the formation of the U phase, in: Scrivener, K.L., Young, J.F. (Eds.),
594 Mechanisms of chemical degradation of cement-based systems. CRC Press, New York, pp.
595 427-435.

596 Li, G., Le Bescop, P., Moranville, M., 1996. The U phase formation in cement-based systems
597 containing high amounts of Na_2SO_4. Cem. Concr. Res. 26, 27-33.

598 Li, G., Le Bescop, P., Moranville-Regourd, M., 1997. Synthesis of the U phase
599 ($4CaO{\cdot}0.9Al_2O_3{\cdot}1.1SO_3{\cdot}0.5Na_2O{\cdot}16H_2O$). Cem. Concr. Res. 27, 7-13.

600 Lidman, F., Kallström, K., Kautsky, U., 2017. Mo-93 from the grave to the cradle. SKB Report
601 P-16-22, 27 pp.

602 Lothenbach, B., Nonat, A., 2015. Calcium silicate hydrates: Solid and liquid phase
603 composition. Cem. Concr. Res. 78, 57-70.

604 Ma, B., Fernandez-Martinez, A., Grangeon, S., Tournassat, C., Findling, N., Claret, F., Koishi,
605 A., Marty, N.C.M., Tisserand, D., Bureau, S., Salas-Colera, E., Elkaïm, E., Marini, C., Charlet, L.,
606 2017. Evidence of multiple sorption modes in layered double hydroxides using Mo as
607 structural probe. Environ. Sci. Technol. 51, 5531-5540.

608 Marty, N.C.M., Grangeon, S., Elkaïm, E., Tournassat, C. Fauchet, C., Claret, F., 2018.
609 Thermodynamic and crystallographic model for anion uptake by hydrated calcium aluminate
610 (AFm): an example of molybdenum. Scientific Reports 8, 7943, DOI:10.1038/s41598-018-
611 26211-z.

612 Matschei, T., Lothenbach, B., Glasser, F.P., 2006. The AFm phase in Portland cement. Cem.
613 Concr. Res. 37, 118-130.

614 Mondal, P., Jeffery, J.W., 1975. The crystal structure of tricalcium aluminate, $Ca_3Al_2O_6$. Acta
615 Crystallogr. B 31, 689-697.

616 Myneni, S.C.B., Traina, S.J., Waychunas, G.A., Logan, T.J. 1998. Vibrational spectroscopy of
617 functional group chemistry and arsenate coordination in ettringite. Geochim. Cosmochim.
618 Acta 62, 3499-3514.

619 Ochs, M., Lothenbach, B., Giffaut, E., 2002. Uptake of oxo-anions by cements through solid-
620 solution formation: experimental evidence and modelling. Radiochim. Acta 90, 639-646.

621 Ochs, M., Mallants, D., Wang, L., 2016. Radionuclide and metal sorption on cement and
622 concrete, Springer, 301 pp.

623 Parkhurst, D.L., Appelo, C.A.J., 2013. Description of input and examples for PHREEQC version
624 3 - A computer program for speciation, batch-reaction, one-dimensional transport, and
625 inverse geochemical calculations: U.S. Geological Survey Techniques and Methods, book 6,
626 chap. A43, 497 p., available at http://pubs.usgs.gov/tm/06/a43.

627 Scatchard, G., 1936. Concentrated solutions of strong electrolytes. Chem. Rev. 19, 309-327.

628 Stöber, S. Pöllmann, H., 2017. Crystallography and crystal chemistry of AFm phases related
629 to cement chemistry. In: Pöllmann, H. (ed.) Cementitious materials - Composition,
630 Properties, Application, de Gruyter, 191-250.

631 Taylor, H.F.W., 1997. Cement chemistry, Thomas Telford, 459 pp.

632 Tits, J., Iijima, K., Wieland, E., Kamei, G., 2006. The uptake of radium by calcium silicate
633 hydrates and hardened cement paste. Radiochim. Acta 94, 637-643.

634 Wang, L., Ochs, M., Mallants, D., Vielle-Petit, L., Martens, E., Jacques, D., de Cannière, P.,
635 Berry, J.A., Leterme, B., (2013). A new radionuclide sorption data base for benchmark
636 cement accounting for geochemical evolution of cement. In: Bart, F., Cau-dit-Coumes, C.,
637 Frizon, F., Lorente, S. (eds.) Cement-based materials for nuclear waste storage, Springer,
638 103-112.

639 Wieland, E., 2014. Sorption data base for the cementitious near field of L/ILW and ILW
640 repositories for provisional safety analyses for SGT-E2. NAGRA Technical Report NTB 14-08,
641 104 pp.

642 Wieland, E., Van Loon, L.R., 2002. Cementitious near-field sorption data base for
643 performance assessment of an ILW repository in Opalinus Clay. NAGRA Technical Report NTB
644 02-20, 87 pp.

645 Wieland, E., Tits, J., Spieler, P., Dobler, J.P., 1998. Interaction of Eu(III) and Th(IV) with
646 sulfate-resisting portland cement. Mater. Res. Soc. Symp. Proc. 506, 573-578.

647 Zhang, M., 2000. Incorporation of oxyanionic B, Cr, Mo, and Se into hydrocalumite and
648 ettringite: application to cementitious systems. PhD thesis, University of Waterloo, 172 pp.

649 Zhang, M., Reardon, E.J., 2003. Removal of B, Cr, Mo, and Se from wastewater by
650 incorporation into hydrocalumite and ettringite. Environ. Sci. Technol. 37, 2947-2952

651

Supplementary Material

Table S1

Specific surface area (SSA) of cement hydration phases and HCP used in the sorption experiments (n.d.: not determined; Lange et al., 2018; Lange, 2019).

Phase	C-S-H 0.9	C-S-H 1.4	AFm-SO_4	AFm-CO_3	Ettringite	C_3AH_6	$Ca(OH)_2$	$CaCO_3$	HCP CEM I
SSA [m^2 g^{-1}]	126	109	1.1	n.d.	13.6	1.5	n.d.	n.d.	24.2

Table S2

pH of aqueous solutions equilibrated with various cement hydration phases and HCP.

	C-S-H 0.9	C-S-H 1.4	AFm-SO_4	AFm-CO_3	Ettringite	C_3AH_6	$Ca(OH)_2$	$CaCO_3$	HCP CEM I
pH_{ini}	11.9±0.2	12.1±0.2	12.0±0.2	11.3±0.2	11.1±0.2	12.1±0.2	12.3±0.2	7.5±0.2	12.6±0.2

Table S3

Final molybdenum concentrations and saturation indices of powellite ($SI_{powellite}$) in the batch sorption experiments to determine steady state R_d values (*cf.* Table 1). The calcium concentrations were obtained by geochemical modelling using PhreeqC.

	C-S-H 0.9	C-S-H 1.4	AFm-SO_4	AFm-CO_3	Ettringite	C_3AH_6	$Ca(OH)_2$	$CaCO_3$
ES								
Mo [mol L^{-1}]	1.14E-07	6.42E-08	2.18E-08	2.17E-08	1.57E-07	1.26E-08	7.37E-07	1.51E-07
Ca [mol L^{-1}]	1.32E-03	2.31E-03	4.54E-03	2.60E-03	2.12E-03	5.37E-03	2.05E-02	1.28E-03
$SI_{powellite}$	-2.27	-2.36	-2.56	-2.65	-1.84	-2.77	-0.73	-2.01
ACW								
Mo [mol L^{-1}]	3.11E-07	4.21E-07	4.87E-07		3.07E-07	1.99E-08		
Ca [mol L^{-1}]	1.93E-03	1.55E-03	2.23E-03		2.06E-03	1.80E-03		
$SI_{powellite}$	-2.67	-2.63	-2.42		-2.65	-3.90		
CH								
Mo [mol L^{-1}]			1.37E-07	6.32E-08	6.32E-07	6.34E-08		1.87E-06
Ca [mol L^{-1}]			2.06E-02	2.05E-02	2.05E-02	2.05E-02		2.05E-02
$SI_{powellite}$			-1.46	-1.80	-0.80	-1.80		-0.33

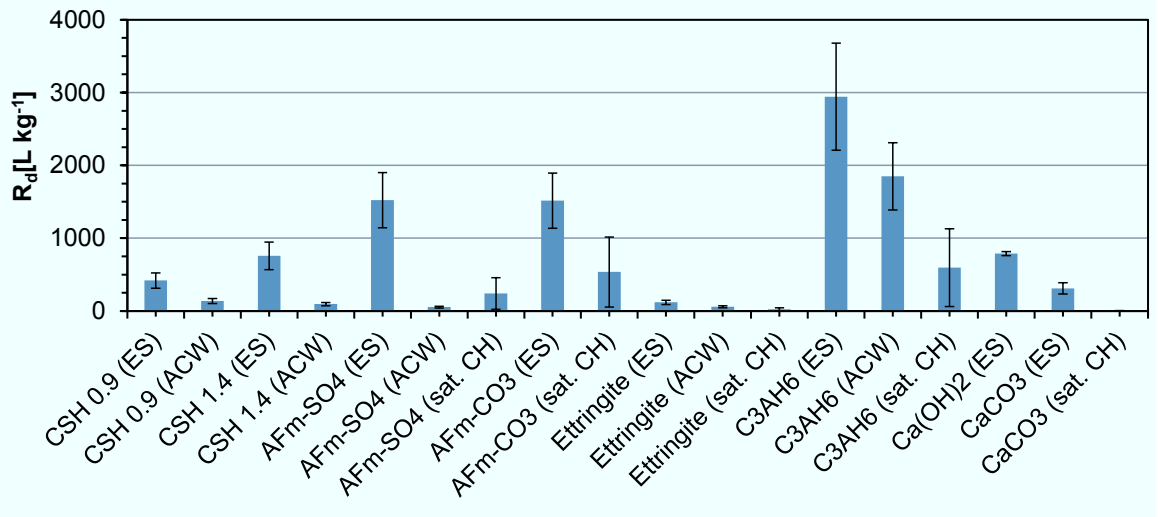

Fig. S1. Distribution ratios R_d for the molybdate uptake by various cement hydration phases in different solutions (ES: equilibrium solution; ACW: artificial young cement water (pH 13.3); CH: portlandite saturated solution (pH 12.3); C_3AH_6: hydrogarnet; duration of experiments: 30 days).

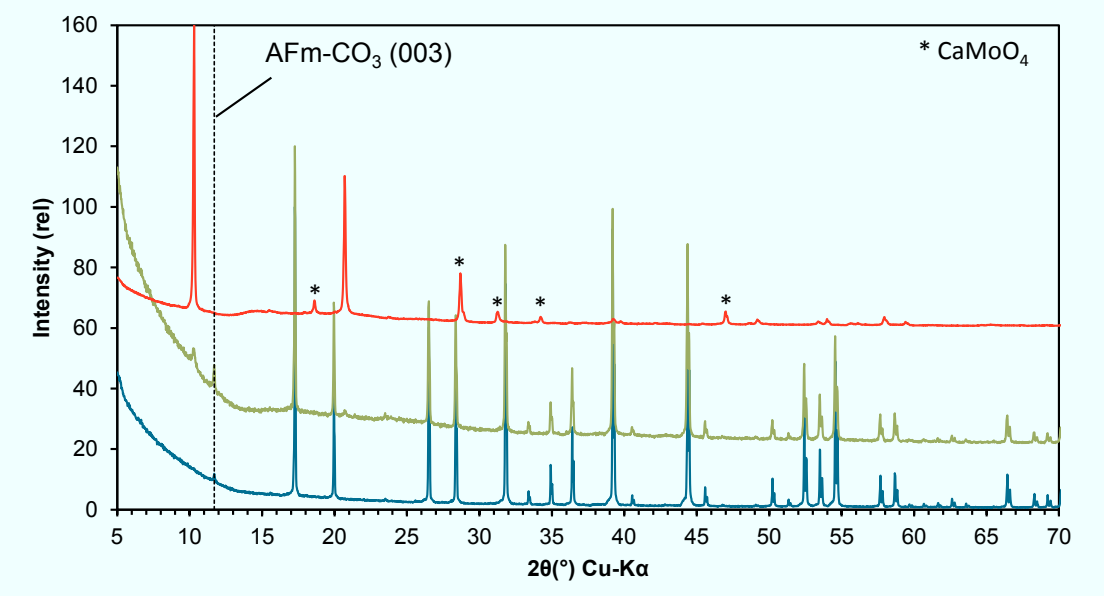

Fig. S2. Comparison of XRD patterns obtained after the termination of molybdate uptake experiments with hydrogarnet (C_3AH_6) at initial MoO_4^{2-} concentrations of 10^{-6} mol L^{-1} (blue) and 10^{-3} mol L^{-1} (green) with the diffraction pattern of AFm-MoO_4 (red), containing some powellite impurities (marked by asterisks).

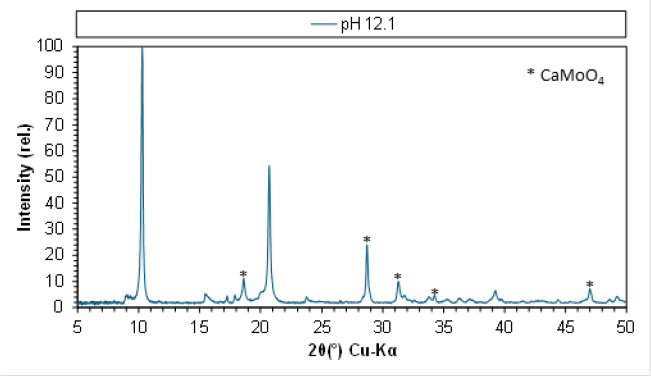

680

681 **Fig. S3.** XRD pattern of AFm-MoO_4 synthesised under alkali-free alkaline conditions (final pH
682 = 12.1) (reflexes marked with an asterisk originate from powellite impurities).